Aalborg Universitet

AALBORG UNIVERSITY

DENMARK

Modeling of Landslides with the Material Point Method

Andersen, Søren Mikkel; Andersen, Lars Vabbersgaard

Published in:
Proceedings of the Sixth International Conference on Engineering Computational Technology

Publication date:
2008

Document Version
Publisher's PDF, also known as Version of record

Link to publication from Aalborg University

Citation for published version (APA):
Andersen, S. M., & Andersen, L. (2008). Modeling of Landslides with the Material Point Method. In M. Papadrakakis, & B. H. V. Topping (Eds.), Proceedings of the Sixth International Conference on Engineering Computational Technology Civil-Comp Press.
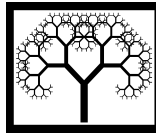
Paper 177

Modeling of Landslides with the Material Point Method

S. Andersen and L. Andersen
Department of Civil Engineering
Aalborg University, Denmark

Abstract

A numerical model for studying the dynamic evolution of landslides is presented. The numerical model is based on the Generalized Interpolation Material Point Method. A simplified slope with a house placed on top is analysed. An elasto-plastic material model based on the Mohr-Coulomb yield criterion is employed for the soil. The slide is triggered for the initially stable slope by removing the cohesion of the soil and the slide is followed from the triggering until a state of equilibrium is again reached. Parameter studies, in which the angle of internal friction of the soil and the degree of discretization is varied, are presented.

Keywords: landslide, soil dynamics, slope stability, material point method.

1 Introduction

As a part of the globalisation, cities are built in mountainous areas in which landslides are common occurrences. If landslides cannot be prevented it is of interest to know the extent of an eventual slide. Landslides are a very complicated and varied physical phenomena depending among other factors on the slope geometry, the soil properties and the environment. An example from the north western Denmark where landslides are naturally shaping the landscape is shown in Figure 1. It shows a church next to an unstable slope. The church was initially centrally placed in a farming community but is now at risk of falling into the sea. The soil consist of vertically interchanging layers of plastic clay and sand. Minor landslides take place after heavy rainfall when saturation reduces the adhesion between the soil layers. Previous research has focused on determining the reliability of slopes and the risk of failure. An overview of the traditional slope-stability analysis using limit equilibrium and finite-element analysis is given by Duncan [1]. The idea in the present paper is, however, to examine the

Figure 1: Landslides on the coast at north-western Denmark.

dynamic evolution of slides in unstable slopes by means of numerical simulations.

The modelling of landslides is performed with the aid of the Generalized Interpolation Material-Point method (GIMP) [2]. The GIMP is an extension of the Material-Point Method (MPM), developed in the 1990s [3, 4]. In the GIMP, two material descriptions are employed. The soil is described using a Lagrangian description in which the soil is divided into a number of discrete material points at which the mass, stresses, strains and other properties are evaluated. This allows for incorporation of complex constitutive material models as history dependent variables are tracked through the simulation. The physical properties are mapped to an Eulerian grid where the kinematic equations are solved. The combination of the Langrangian and the Eulerian material description allows the simultaneous modelling of complex material behaviour and large displacements. The mapping between the material points and the grid is provided by mapping functions. Initial simulations based on the standard MPM formulation with linear shape-functions and hence discontinuous gradients has been tried. However, this formulation fails to model the stress-distribution in the slope that varies continuously with the dept. The GIMP combines shape-functions associated with the mesh with particle characteristic functions associated with the material points. The result are smooth mapping functions with continuous gradients that are able to model the stress distributions in the slope. The GIMP formulation has been tested against other higher-order mapping schemes such as interpolation using cubic splines. The GIMP method models the slope stresses in a smoother and more realistic fashion than the

cubic-spline interpolation, probably due to the more compact support. The simulation procedure is as follows:

- Stresses are determined for a stable slope

- A landslide is triggered

- The dynamical evolution of the slide is modelled.

The initial stress distribution in the slopes are determined using incremental gravitation. The dynamical simulation is performed using explicit time integration. The Jaumann stress rate tensor is employed to ensure an objective stress rate while a logarithmic expression is used to model changes in density. The constitutive behaviour of the soil is described by an elasto-plastic material model based on the Mohr-Coulomb yield criterion. A method for efficient return mapping is employed [8].

The test case is a landslide triggered by the cohesion of soil the being removed. This is a typical scenario after heavy rainfall in fine-grained soils. The extent of the slide is determined for different types of soil. The purpose of the analysis is to provide a further understanding of the dynamical evolution of landslides in different soil types.

2 Defining the problem

For urban environments built close to or on mountains and steep slopes it is important to know the behaviour of an eventual landslide. This also applies to city developers planning to construct buildings for residential of commercial use near to or on a slope. Examples of recent landslides includes rainfall-induced landslides in Hong Kong [5], debris flows in Nantou County, Taiwan, due to typhoons [6] and debris flow due to decementation because of rainfall and weathering in Brazil [7]. A characteristic scenario is shown in Figure 2.

These kinds of scenarios are analysed in this article by the aid of the Generalized Material Point Method which is described in the next section.

3 The Generalized Material Point Method

A continuum material subject to initial and boundary conditions is considered. The initial computational domain is denoted Ω_0. At the time t the domain is denoted $\Omega(t)$. The boundary $\partial\Omega$ is divided into two disjoint sets: $\partial\Omega_u$ with prescribed displacements and $\partial\Omega_\tau$ with known traction. The governing equations are balance of momentum, mass conservation, and conservation of energy. Firstly, conservation of mass implies that

$$\frac{d\rho}{dt} + \rho\nabla \cdot \mathbf{v} = 0, \tag{1}$$

Rainfall

Unstable soil material

Exposed House

Before the slide

Initiation of failure
surface

Scenario 1

The house is not hit by the landslide

Scenario 2

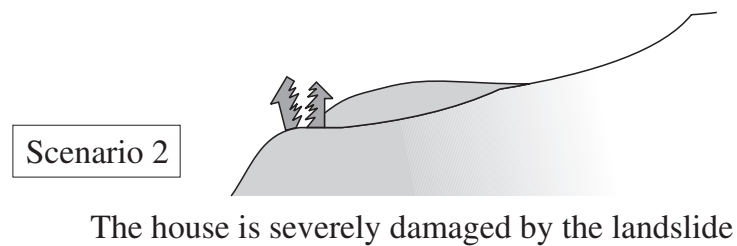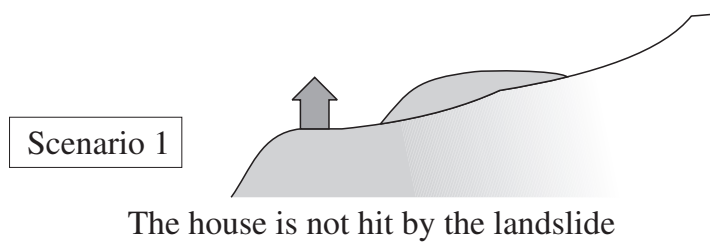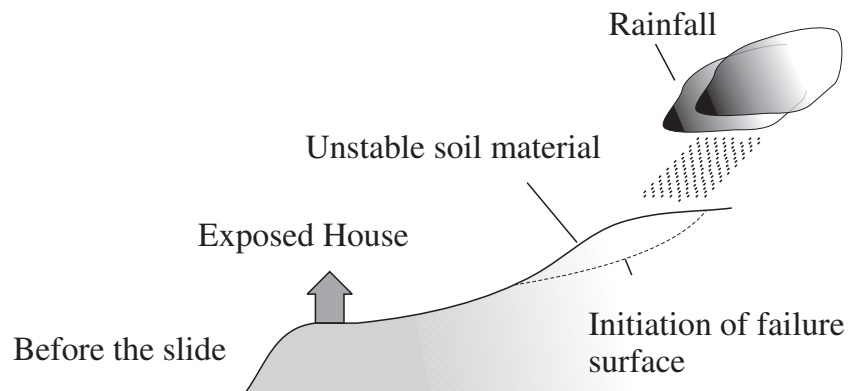The house is severely damaged by the landslide

Figure 2: A house built next to an unstable slope.

where $\mathbf{v} = \mathbf{v}(\mathbf{x}, t)$ is the material velocity and $\rho = \rho(\mathbf{x}, t)$ is the current density. Further, ∇ is the gradient operator and $\nabla \cdot \mathbf{a}$ is the divergence of the vector field $\mathbf{a}$. Secondly, conservation of momentum involves that

$$\rho \frac{d\mathbf{v}}{dt} = \nabla \cdot \boldsymbol{\sigma} + \rho \mathbf{b}, \tag{2}$$

where $\boldsymbol{\sigma} = \boldsymbol{\sigma}(\mathbf{x}, t)$ is the Cauchy stress tensor and $\mathbf{b} = \mathbf{b}(\mathbf{x}, t)$ is the specific body force. Finally, energy conservation is ensured by the equation

$$\rho \frac{dE}{dt} = \boldsymbol{\sigma} : \frac{d\boldsymbol{\varepsilon}}{dt} + \rho \mathbf{v} \cdot \mathbf{b}, \tag{3}$$

where E is the internal energy per unit mass in the current configuration, $\boldsymbol{\varepsilon} = \boldsymbol{\varepsilon}(\mathbf{x}, t)$ is the strain and $d\boldsymbol{\varepsilon}/dt$ the corresponding strain rate.

By discretization of the continuum problem, the material is divided into a finite number of material points. Each material point is assigned a mass, velocity, acceleration, stress, strain and other relevant properties defining the state of the material. As the mass is carried by the material points, the conservation of mass is automatically satisfied. Equation (2), defining the balance of momentum is solved by discretization of its weak form. The energy balance can then afterwards be used as an auxiliary equation to estimate the accuracy of the model.

In order to obtain the weak form of the balance of momentum, Equation (2) is multiplied by an arbitrary test function $\mathbf{w}$ and integrated over the domain. By application of the Green theorem, the balance becomes:

$$\int_\Omega \rho \mathbf{w} \cdot \frac{d\mathbf{v}}{dt} d\Omega = \int_{\partial\Omega_\tau} \mathbf{w} \cdot \boldsymbol{\tau} dS - \int_\Omega \frac{\partial \mathbf{w}}{\partial \mathbf{x}} : \boldsymbol{\sigma} d\Omega + \int_\Omega \rho \mathbf{w} \cdot \mathbf{b} d\Omega, \tag{4}$$

where $\boldsymbol{\tau} = \boldsymbol{\sigma} \cdot \mathbf{n}$ is the surface traction and $\mathbf{n}$ is the outward unit normal to the material surface in the current configuration.

The density field is discretized using particle characteristic functions. The mass assigned to each material point can be expressed as

$$m_p = \int_{\Omega_0} \rho_0(\mathbf{x}) \chi_p(\mathbf{x}) d\Omega_0, \tag{5}$$

where m_p is the mass associated with material point p, $\rho_0(\mathbf{x})$ is the initial density field and $\chi_p(\mathbf{x})$ is the particle characteristic function associated with the material point. The particle functions are defined such that they are a partition of unity in the initial configuration, i.e.

$$\sum_p \chi_p(\mathbf{x}_0) = 1 \ \forall \ \mathbf{x}_0 \tag{6}$$

Further, the stress at a material point is given by

$$\boldsymbol{\sigma}_p^0 = \frac{1}{V_p^0} \int_{\Omega_0} \boldsymbol{\sigma}^0(\mathbf{x}) \chi_p(\mathbf{x}) d\Omega_0. \tag{7}$$

The material velocity and acceleration is represented continuously on the grid by means of nodal shape functions. Defining a finite number N_n of grid nodes, the velocity and acceleration field are represented as

$$\mathbf{v}(\mathbf{x},t) = \sum_{i=1}^{N_n} \Phi_i(\mathbf{x})\mathbf{v}_i(t) \tag{8}$$

and

$$\frac{d\mathbf{v}}{dt} = \sum_{i=1}^{N_n} \Phi_i(\mathbf{x})\frac{d\mathbf{v}_i}{dt}, \tag{9}$$

where $\Phi_i(\mathbf{x})$ is the nodal shape function associated with node i while $\mathbf{v}_i(t)$ and $d\mathbf{v}_i/dt$ are the nodal velocity and acceleration respectively. Similarly the nodal shape functions are used to represent the field of admissible test functions:

$$\mathbf{w}(\mathbf{x},t) = \sum_{i=1}^{N_n} \Phi_i(\mathbf{x})\mathbf{w}_i(t). \tag{10}$$

Substituting Equations (5) to (10) into the balance of momentum and utilizing that the test functions are arbitrary yield the set of equations

$$\sum_{i=1}^{N_n}\sum_{p=1}^{N_p} \dot{\mathbf{p}}_p \frac{1}{V_p} \int_{\Omega_p \bigcap \Omega_i} \chi_p(\mathbf{x})\Phi_i(\mathbf{x})d\Omega = i = 1^{N_n} \int_{\partial\Omega} \Phi_i(\mathbf{x})\boldsymbol{\tau}dS$$

$$-\sum_{i=1}^{N_n}\sum_{p=1}^{N_p}\boldsymbol{\sigma}_p \int_{\Omega_p \bigcap \Omega_i} \chi_p(\mathbf{x})\frac{\partial\Phi_i}{\partial\mathbf{x}}d\Omega + \sum_{i=1}^{N_n}\sum_{p=1}^{N_p} m_p\mathbf{b}_p\frac{1}{V_p} \int_{\Omega_p \bigcap \Omega_i} \chi_p(\mathbf{x})\Phi_i(\mathbf{x})d\Omega \tag{11}$$

where $\dot{\mathbf{p}}_p = d\mathbf{p}_p/dt = m_p d\mathbf{v}_p/dt$ is the material time derivative of the momentum and V_p is the current volume of the particle. Introducing the weighting function and the gradient weighting function as

$$S_{ip} = \frac{1}{V_p} \int_{\Omega_p \bigcap \Omega_i} \chi_p(\mathbf{x})\Phi_i(\mathbf{x})d\Omega \tag{12}$$

and

$$\nabla S_{ip} = \int_{\Omega_p \bigcap \Omega_i} \chi_p(\mathbf{x})\frac{\partial\Phi_i}{\partial\mathbf{x}}d\Omega \tag{13}$$

respectively, yields the discrete equations

$$\dot{\mathbf{p}}_i = \mathbf{f}_i^{int} + \mathbf{f}_i^{ext}, \tag{14}$$

where $\dot{\mathbf{p}}_i$ is the rate of change of the nodal momentum , $\mathbf{f}_i^{int}$ is the vector of internal forces and $\mathbf{f}_i^{ext}$ is the vector of external forces defined respectively as

$$\dot{\mathbf{p}}_i = \sum_{p=1}^{N_p} S_{ip}\dot{\mathbf{p}}_p, \tag{15}$$

6

$$\mathbf{f}_i^{int} = -\sum_{p=1}^{N_p} \boldsymbol{\sigma}_p \cdot \nabla S_{ip} V_p, \tag{16}$$

$$\mathbf{f}_i^{ext} = \sum_{p=1}^{N_p} m_p \mathbf{b} S_{ip} + \int_{\partial\Omega_\tau} \Phi_i(\mathbf{x})\boldsymbol{\tau} dS. \tag{17}$$

4 Constitutive models

The strain rate is represented on the background grid as

$$\dot{\varepsilon}(\mathbf{x}) = \frac{1}{2}(\nabla\mathbf{v}(\mathbf{x}) + (\nabla\mathbf{v}(\mathbf{x}))^T) = \frac{1}{2}(\nabla\Phi_i\mathbf{v}_i + \mathbf{v}_i^T\nabla\Phi_i^T). \tag{18}$$

This is utilised to find the particle strain rate as a volume-weighted average over each particle:

$$\dot{\boldsymbol{\varepsilon}}_p = \frac{1}{V_p}\int_{\Omega_p\cap\Omega_i}\chi_p(\mathbf{x})\dot{\varepsilon}(\mathbf{x})d\Omega = \sum_{i=1}^{N_n}\frac{1}{2}(\nabla S_{ip}\mathbf{v}_i + \mathbf{v}_i^T\nabla S_{ip}^T). \tag{19}$$

The strain rates are used to find the stress rates which integrated in time determine the stress. An elasto-plastic material model based on the Mohr-Coulomb yield function is employed. Non-associated plasticity is assumed. A yield function f is introduced such that $f < 0$ corresponds to elastic material behaviour and elasto-plastic behaviour is observed when $f = 0$. The yield criterion is given in terms of the Mohr-Coulomb yield function defined in terms of the principal stresses by

$$f = \frac{1}{2}(\sigma_3 - \sigma_1) + \frac{1}{2}(\sigma_1 + \sigma_3)\sin(\phi) - c\cos(\phi), \tag{20}$$

where ϕ is the angle of friction and c is the cohesion. In Equation (20) tension is considered positive and the principal stresses are ordered as $\sigma_1 \leq \sigma_2 \leq \sigma_3$. The stress rate is given in terms of the elastic strain rate

$$\dot{\boldsymbol{\sigma}} = \mathbf{E} : (\dot{\boldsymbol{\varepsilon}} - \dot{\boldsymbol{\varepsilon}}^p), \tag{21}$$

where $\dot{\boldsymbol{\varepsilon}}$ is the total strain rate, $\dot{\boldsymbol{\varepsilon}}^p$ is the plastic rate and $\mathbf{E}$ is the elastic constitutive tensor. The plastic strain increment is found using the relation

$$\dot{\boldsymbol{\varepsilon}}^p = \dot{\lambda}\frac{\partial g}{\partial\sigma_{\alpha\beta}}, \tag{22}$$

where $\dot{\lambda}$ a positive scaling factor and the g is the plastic potential function given by

$$g = \frac{1}{2}(\sigma_3 - \sigma_1) + \frac{1}{2}(\sigma_1 + \sigma_3)\sin(\psi), \tag{23}$$

where ψ is the angle of dilatation of the soil. In the numerical solution, finite increments in the strain are considered. Hence, the state of stress may initially be taken outside the yield surface. An efficient return of the stresses back to the yield surface is obtained by the algorithm proposed by Clausen et al. [8].

Further, in order to accommodate the large deformations taking place in the model, the Jaumann stress-rate tensor is introduced as

$$\breve{\boldsymbol{\sigma}} = \dot{\boldsymbol{\sigma}} + tr(\dot{\boldsymbol{\varepsilon}})\boldsymbol{\sigma} - \dot{\boldsymbol{\varepsilon}}\boldsymbol{\sigma} - \boldsymbol{\sigma}\dot{\boldsymbol{\varepsilon}}, \tag{24}$$

where $\dot{\boldsymbol{\sigma}}$ is the stress rate determined from Equation (21) and $\breve{\boldsymbol{\sigma}}$ is the objective Jaumann stress rate. The expressions are given in terms of the current particle volume. The volume is determined by $V_p = m_p/\rho_p$. Separation of the variables in the equation of mass (1) and integrating in time from t^k to t^{k+1} yields

$$\rho^{k+1} = \rho^k e^{-\nabla \cdot \mathbf{v}\Delta t}, \tag{25}$$

where $\Delta t = t^{k+1} - t^k$ is the time step. The term $\nabla \cdot \mathbf{v}$ is found using the gradients of the weighting functions.

5 GIMP calculation procedure

The problem is integrated in time using a dynamical scheme where the information is carried by the material points. Initially, the system is discretized by a set of material points $p = 1...N_p$. The mass at grid node i at time step k is found by

$$m_i^k = \sum_{p=1}^{N_p} m_p^k S_{ip}, \tag{26}$$

and the momentum at grid node is found by

$$\mathbf{p}_i^k = \sum_{p=1}^{N_p} \mathbf{p}_p^k S_{ip}. \tag{27}$$

Using a forward difference and integrating Equation (14) over a time step yields

$$\mathbf{p}_i^{k+1} = \mathbf{p}_i^k + \Delta t(\mathbf{f}_i^{int,k} + \mathbf{f}_i^{ext,k}). \tag{28}$$

The position and velocity updates for the material points are given by

$$\mathbf{x}_p^{k+1} = \mathbf{x}_p^k + \Delta t \sum_{i=1}^{N_n} \frac{1}{m_i^k} \mathbf{p}_i^{k+1} S_{ip} \tag{29}$$

and

$$\mathbf{v}_p^{k+1} = \mathbf{v}_p^k + \Delta t \sum_{i=1}^{N_n} \frac{1}{m_i^k} (\mathbf{f}_i^{int,k} + \mathbf{f}_i^{ext,k}) S_{ip} \tag{30}$$

Further, the strain rates are replaced by a finite strain increment,

$$\Delta\varepsilon_p = \frac{\Delta t}{2}\sum_{i=1}^{N_n}(\nabla S_{ip}^k \mathbf{v}_i^k + (\mathbf{v}_i^k)^T(\nabla S_{ip}^k)^T), \tag{31}$$

and the corresponding stress increment is found according to the constitutive model. In the simulations in this paper, a constant time step is employed. The complete GIMP algorithm is given by:

- Initialisation of state variables at the material points at time $t^0 = 0$

- At each time step

    - A background computational grid is generated
    - The weighting and gradient weighting functions are determined
    - The nodal mass and momentum is determined according to Equations (26) and (27)
    - The strain-increments are calculated by Equation (31)
    - Stress increments are found according to the constitutive model
    - Strains and stresses are updated
    - The internal and external force vectors are found by Equations (16) and (17), respectively
    - The position and velocity of the material points are found by Equations (29) and (30), respectively
    - The updated densities of the material points are found by Equation (25).

Updating the stresses and strains before calculation of internal forces is shown by Bardenhagen, [9], to the have better energy preserving properties than updating the stresses after calculation of internal forces. Further integrating in terms of momentum and mapping only the changes is shown by Sulsky et al. [4] to yield the best results when implemented numerically. Hence, these solutions have been applied in the present analysis.

6 Determining the stress distribution in stable slopes

In order to model the initiation of slope failure according to the Mohr-Coulomb yield criterion, the stress distribution in the slope must be known in the initial state of static equilibrium. In the test cases presented in this paper, this has been accomplished by modelling an initially stable slope satisfying $f < 0$ at all points. The test case is a slope with uniform slope angle and with a house on top of the slope. The domain is divided into a number of material points representing the soil and the house, respectively, as shown in Figure 3 for a model consisting of 8370 material points.
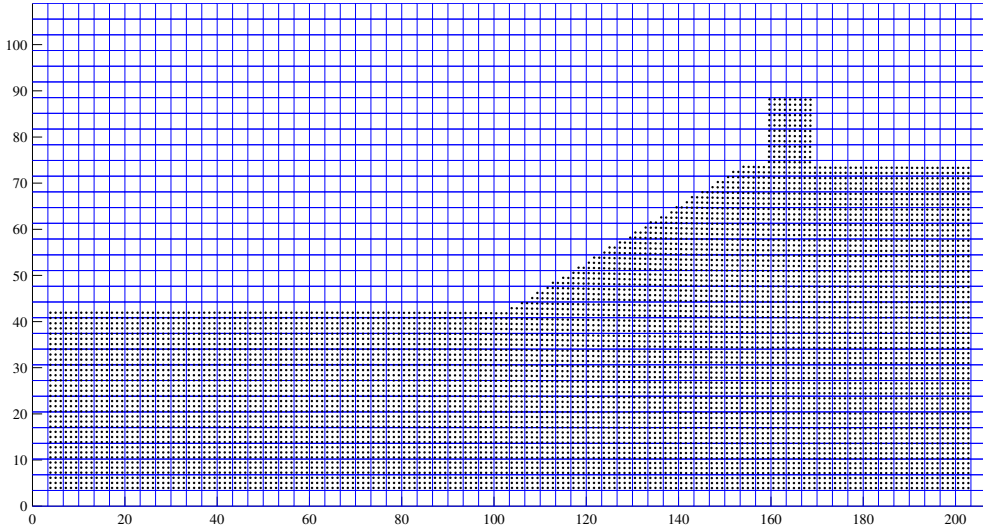
Figure 3: Initial configuration of material points. For the material points modelling the house, a linear elastic material model is used, while a Mohr-Coulomb models is employed for the soil points

At the lower boundary, a rigid boundary is prescribed by enforcing a velocity equal to zero at the grid nodes. At the vertical boundaries, horizontal velocities equal to zero are enforced. As the interpolation is made from the grid nodes to material points extra, initially empty, cells are introduced at the boundaries, in order to avoid that the material points move such that the particle characteristic functions are evaluated outside the grid domain.

An incremental gravitation model is employed. The gravity field is gradually applied as external body forces in Equation (17). A scheme has been employed in which the gravity is applied over a period T. The gravity is linearly increased from $t = 0$ to $t = T/2$ and then maintained constant until $t = T$ as seen in Figure 4. In order to avoid oscillations, a damping scheme is applied by $\mathbf{v}_p^{k+1} := \mathbf{v}_p^{k+1}/(1 + \theta)$. The simulations presented have been performed using $\theta = 0.01$.

The cases presented have all been performed using the geometry depicted in Figure 3. The angle of the slope is $40°$. All the simulations presented have been performed with the following set of material properties.

- $E = 20 MPa$, $\nu = 0.25$

- $\rho_{soil}^0 = 2000 kg/m^3$, $\rho_{house}^0 = 500 kg/m^3$

- $\psi = 10°$.

The simulations have been performed using two by two material points per cell in the initial configuration. Normal stresses in the vertical direction and the horizontal displacements for the simulation using 8730 material points are shown in Figures 5 and
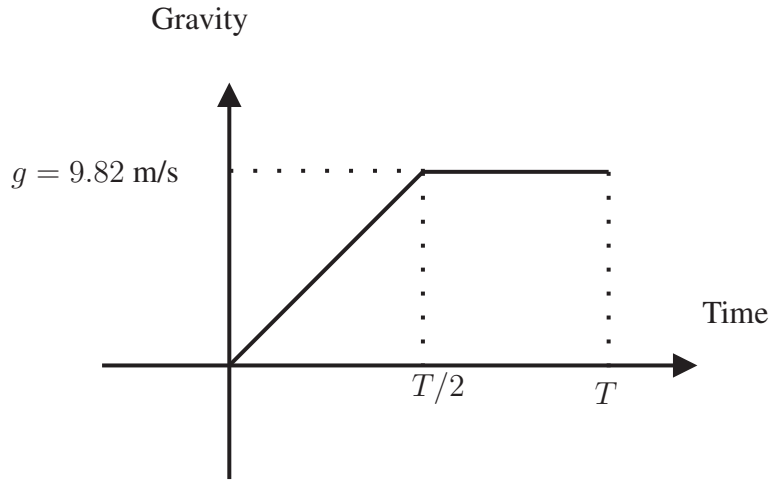
10

Figure 4: Incrementation of gravity over the time period T.

6, respectively. Similarly, Figures 7 and 7 shows the vertical normal stress and the horizontal displacements obtained by the FEA code ABAQUS [10] using quadratic spatial interpolation. Comparison with Figures 5 and 6 leads to the conclusion that the GIMP scheme described above provides initial displacements and stress distribution of an adequate accuracy. Hence, the calculation of quasi-static stresses using GIMP is chosen, primarily because application of commercial finite-element or finite-difference software would require a postprocessing of the results in order to find the stresses at the material points.

7   Numerical results

7.1   Reduction of the cohesion

A soil with both friction and cohesion is considered. Failure in the slope is modelled by removing the cohesion, hence causing plastic material response in the soil according the the yield criterion. This effect of sudden removal of cohesion is present in slopes that are subjected to saturation during heavy rainfall. When a fine-grained frictional soil is partially saturated, an apparent cohesion is present due to capillary tension between the grains. When the soil reaches full saturation, this apparent cohesion is removed and the strength of the soil is reduced. This type of slide can typically take place in mountainous regions in the form of avalanche-like mudslides. In this test case this effect is modelled in a very simple fashion by removing the cohesion of the entire soil simultaneously. After the destabilisation, the soil has a friction angle of $\phi = 20°$. The horizontal displacements 4, 8, 12 and 16 seconds into the landslide are shown in Figure 9. The slide starts by initiation of failure in the slope which at $t = 0$ has a zero velocity. The slide last about 16 seconds with the most rapid phase occurring between 10 and 12 seconds. After an initial redistribution of stresses, due
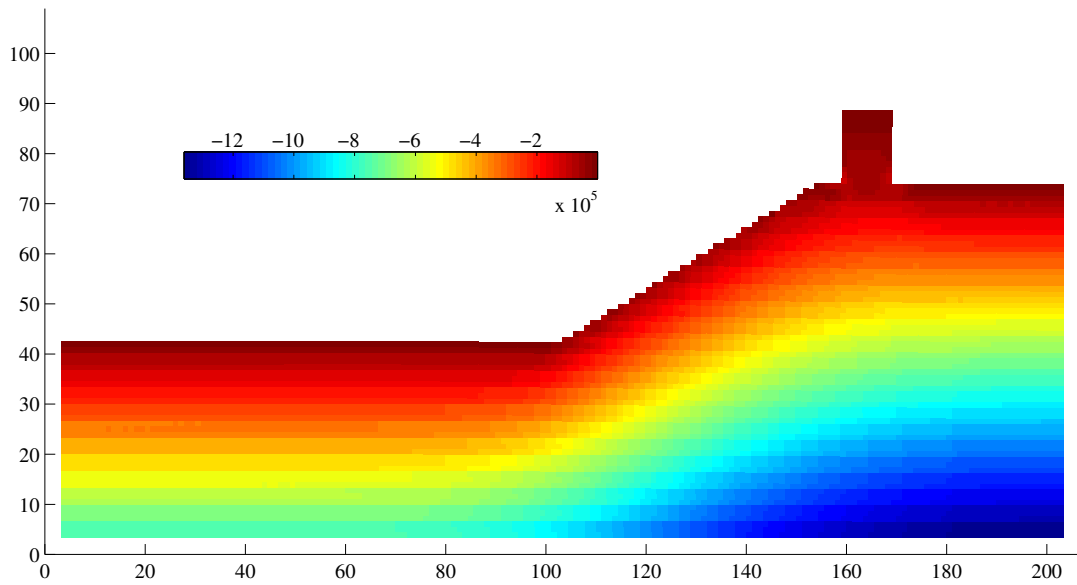
11

Figure 5: Vertical normal stresses in the slope before initiation of failure. 8370 material points. Colours denote stresses in Pa, while the axes are in metres.
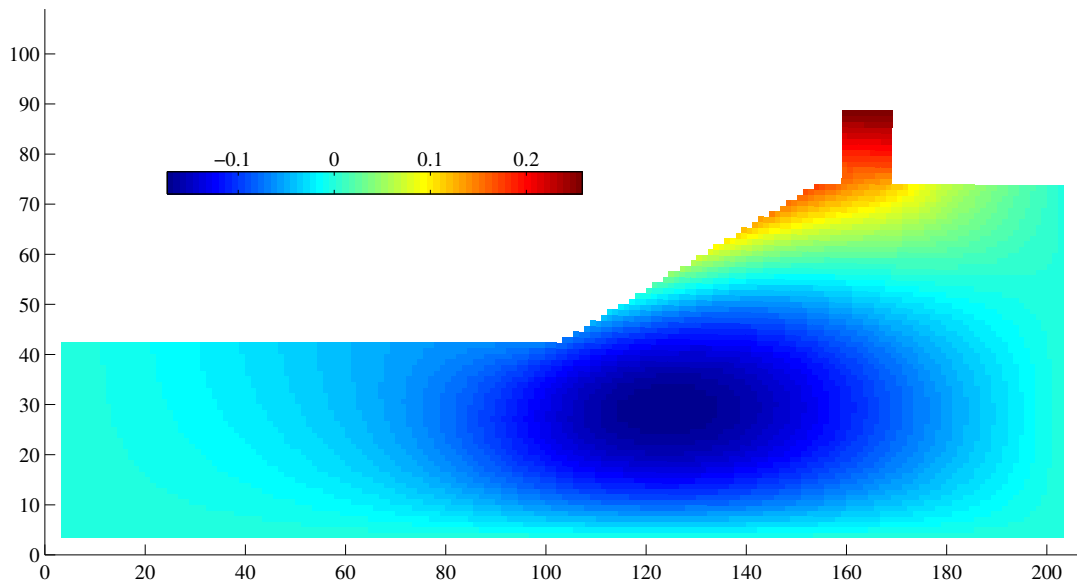

Figure 6: Horizontal displacements due to gravity on the slope before initiation of failure. 8370 material points. Colours denote displacements in metres relative to the unstressed reference state, i.e. before the application of gravity.
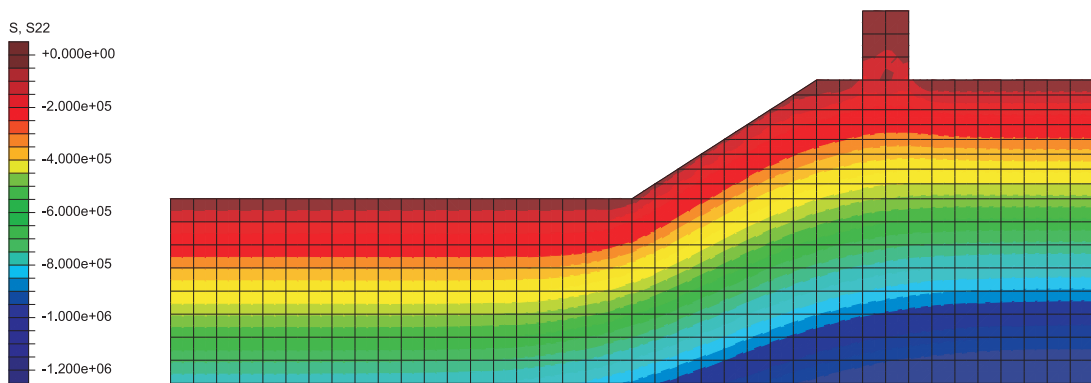
Figure 7: Vertical normal stresses on the slope due to gravity obtained by ABAQUS.
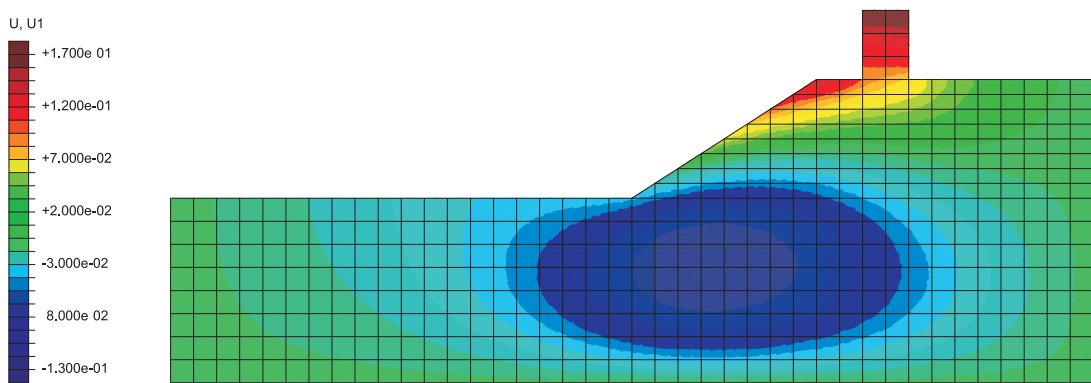

Figure 8: Horizontal displacements due to gravity on the slope obtained by ABAQUS.
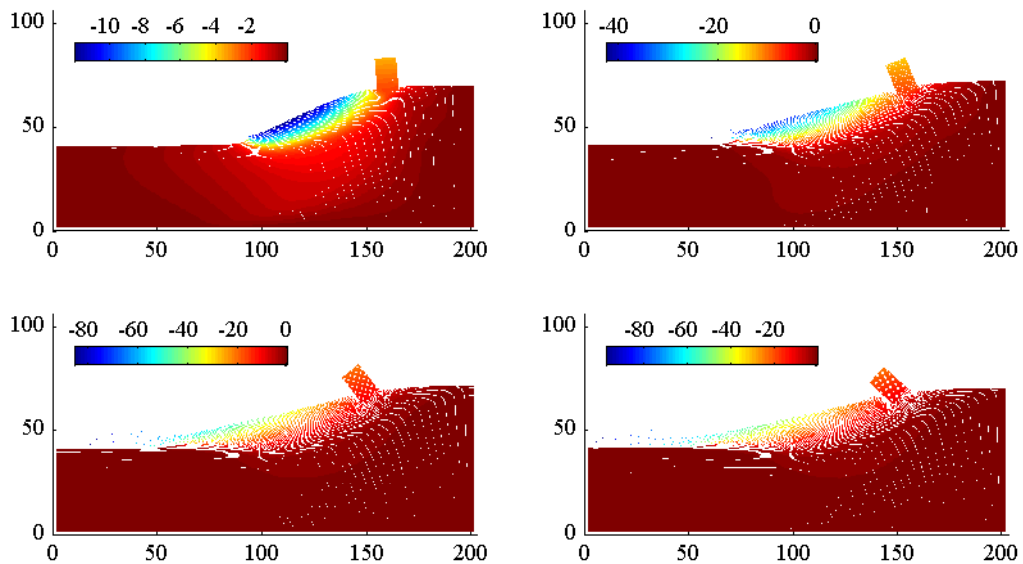

Figure 9: Horizontal displacements in the slope as a function of time in a simulation with 40038 material points. Upper left: 4 s; upper right: 8 s; lower left: 12 s and lower right: 16 s.
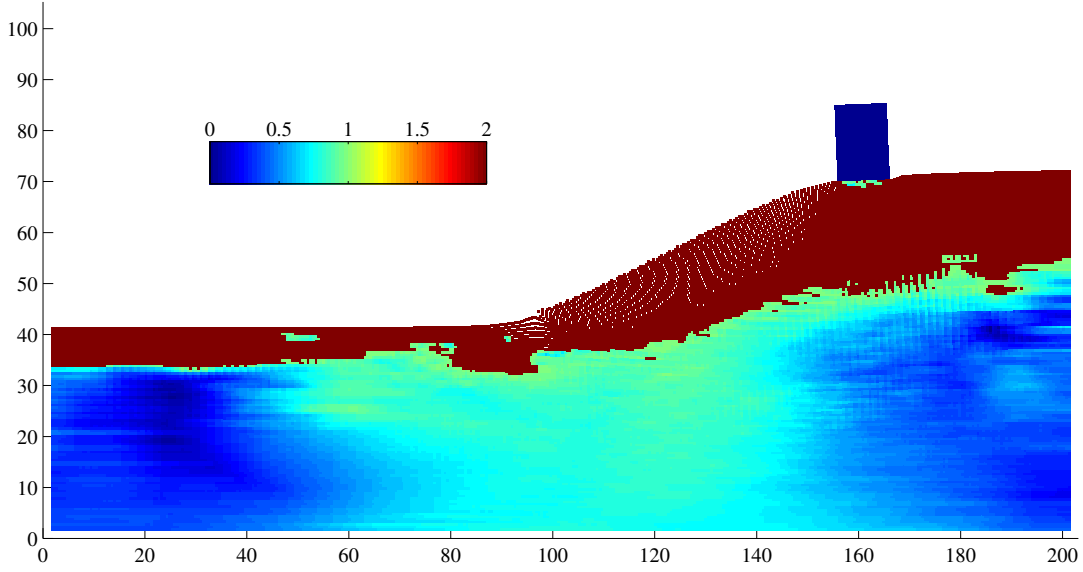
13

Figure 10: The relative stress distribution in the slide 3 seconds into the slide. A value of 2 means plastic yielding, while a value between 0 and 1 corresponds to the relative yield function defined by Equation (32). 40038 material points are used.

to the modelled sudden decrease in strength, a failure surface is generated in the soil. Normalising the yield function, Equation (20), with respect to the material strength yields,

$$f_{rel} = \frac{\frac{1}{2}(\sigma_1 - \sigma_3)}{\frac{1}{2}(\sigma_1 + \sigma_3)\sin(\phi) - c \cdot \cos(\phi)}. \tag{32}$$

Defined in this way, $f_{rel} = 1$ corresponds to yielding while $f_{rel} = 0$ corresponds to a hydrostatic stress state. The relative yielding is illustrated in Figure 10 where a value of two means yielding while a value between zero and one is an expression of the relative stress state.

7.2 Parameter study

In order to understand better how the discretization of the domain influences the solution, simulations with different numbers of material points have been performed. As seen from Figure 11, the results are influenced by the number of material points. The three simulations with 8370, 28724 and 67016 material points, respectively, provide similar results regarding the movement in the large bulk of soil material. However for the local phenomena, i.e. the material points separating from the bulk of moving soil and the interaction between the house and the soil, more realistic results are obtained by the model with 67016 material points. This suggest the implementation of adaptive meshing and distribution of material points, which has not been carried out in this analysis. Based on Figure 11, it is further noted that the interaction between the house and the soil is modelled automatically by the algorithm, while implementing
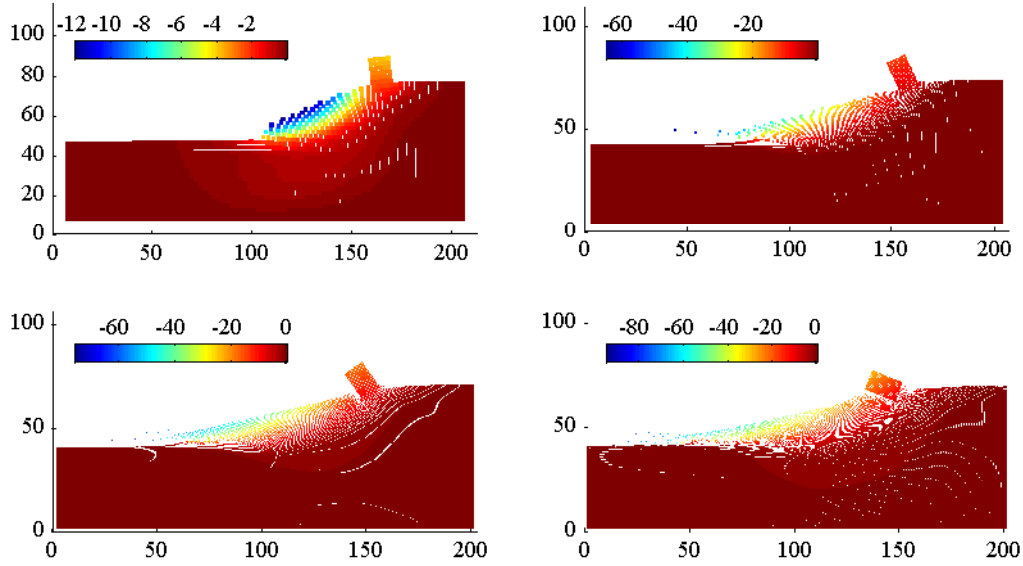
Figure 11: The horizontal displacements in the slope at the end of the slide. Upper left: 1648 material points, Upper right: 8370 material points, Lower left: 28724 material points and Lower right: 67016 material points.

this with other methods is nontrivial. For instance, in the finite-element method the interfaces must be described explicitly in order to account for the interaction between the soil and the house. Processes where new free surfaces are formed and parts of the soil are separating during the collapse of the soil also need to be modelled explicitly. This is the case Lagrangian as well as Eulerian finite-element schemes as well as Arbitrary Lagrangian Eulerian (ALE) finite-element schemes. In contrast the GIMP algorithm automatically determines which material points are interacting through the background grid.

Another feature to note from the parameter study is that after the landslide has occurred, a new stable slope is obtained with a slope angle lower than the angle of friction, due to the initial forces during the landslide.

In the second parameter study, the effects of the material strength on the landslide behaviour are analysed. Four simulations for slopes of uniform strength have been performed. Simulations are carried out with soil with angles of internal friction of $25°$, $20°$, $15°$ and $10°$ respectively. Horizontal displacements at the end of the slides relatively to the reference state are shown in Figure 12. Clearly, the angle of internal friction has a decisive role in the behaviour of the soil during the slide. In the landslide with $\phi = 25°$ the soil is moving slowly as a uniform bulk material without material points separating from the bulk and this landslide is of significantly smaller extent than the others. For the slides with friction angles of $20°$ and $15°$, respectively, material points are separating and sliding on the horizontal soil surface due to inertial forces. In the landslide with $\phi = 10°$ the soil has an almost liquid-like behaviour. The accumulation of material points on the left edge is due to the boundary condition on
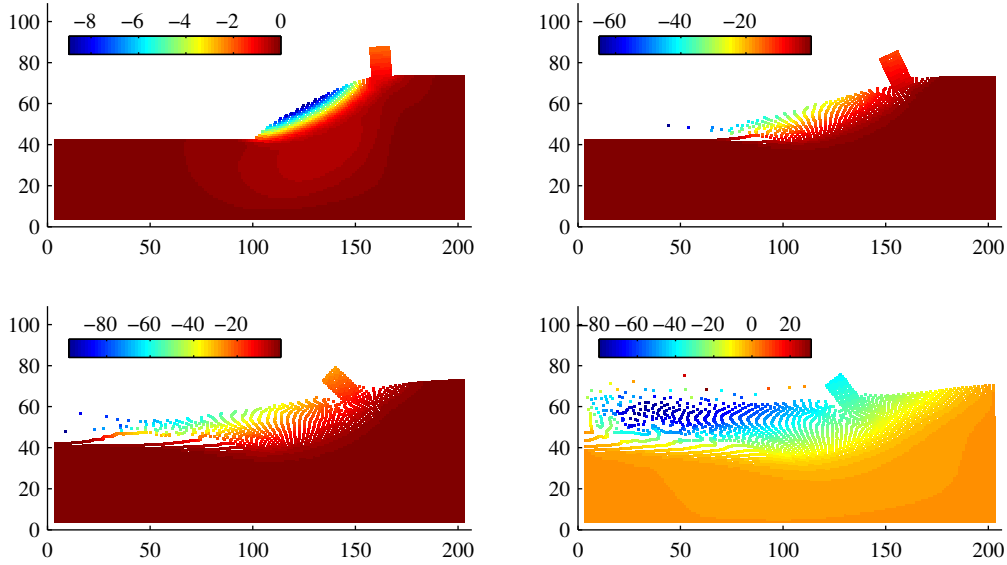
15

Figure 12: The horizontal displacements in the slope at the end of the slide. Simulation using 8370 material points. Upper left: $\phi = 25°$, Upper right: $\phi = 20°$, Lower left: $\phi = 15°$ and Lower right: $\phi = 10°$.

the grid, expressed as $u_x = 0$. Hence, the soil has hit the boundary and some material points have flowed back towards the house. The figure shows that, with the presented numerical model, it is possible to capture qualitatively the behaviour of many different soil materials. Comparison of the model with actual landslides has not been performed but ma be the focus of future research.

Finally, two pitfalls with the current implementation are discussed. The first involves the integration of the weighting functions used for transferring information between the background grid and the material points. In this implementation the weighting functions are found using bilinear products of the analytical expressions for the one-dimensional case derived by Bardenhagen [2]. For the extreme displacements, a consistent integration needs to take into account the rotation and strains of the material points. Hence, particle characteristic functions are not integrated over the current material volume. The other pitfall in the models is associated with the use of an elasto-plastic material model for the extreme deformations. In the parts of the slides involving extreme soil distortions, the soil in reality starts behaving like a fluid or granular flow. Hence, a more complete model needs to model the constitutive behaviour of this soil state in a better way.

8 Conclusions

A numerical framework for modelling landslides based on the Generalized Interpolation Material Point Method has been presented. The approach has been to model the

collapse of slopes in a dynamical time-space model. Slopes with a simplified geometry and initial elastic material behaviour have been made unstable by reducing the strength of the soil. Hence, the slides modelled are similar to mudslides, in which cohesion in slopes is removed due to saturation. The quasi-static stress distributions in the slopes prior to collapse has been determined using the GIMP framework providing results in agreement with commercial FEA programs.

The combination of a Lagrangian material description and a Eulerian grid has made it possible to implement an elasto-plastic material model undergoing large deformations. Further, the interaction of different materials is automatically handled, which has made it possible to model the interaction of collapsing soil slopes and a house build next to the slope. Different parameter studies have been carried out. It has been shown that the obtained solution is dependent of the number of material points used to model the slope. For finely discretized models it has been possible to model local features of the landslide such as material points separating from the slide due to inertial forces in the slide and to model the local collapse of the soil around the house due to distortion of the soil. Finally, a parameter study has been carried out, in which landslides in materials with different angles of friction have been modelled. For relatively high angles of friction, the soil moves as a bulk material and a new stable slope is established with an angle corresponding to the angle of friction. For low angles of friction, the soil behaves almost like a liquid. In this case the soil surface in the final stable state is nearly horizontal.

References

[1] J.M. Duncan, "State of the art: Limit equilibrium and finite-element analysis of slopes", Journal of Geotechnical Engineering, 577-596, 1996.

[2] S.G. Bardenhagen, E.M. Kober, "The Generalized Interpolation Material Point Method", CMES, 5, 477-495, 2004.

[3] D. Sulsky, Z. Chen, H.L. Schreyer, "A particle method for history-dependent materials", Computer Methods in Applied Mechanics and Engineering, 118, 179-196, 1994.

[4] D. Sulsky, S.J. Zhou, H.L Schreyer, "Application of a particle-in-cell method to solid mechanics", Computer Physics Communications, 87, 236-252, 1995.

[5] H. Chen, C.F. Lee, "A dynamic model for rainfall-induced landslides on natural slopes", Geomorphology, 51, 269-2885, 2004.

[6] C. Chien-Yuan, Y. Fan-Chieh, L. Sheng-Chi, C. Kei-Wai, "Discussion of Landslide Self-Organized Critically and the Initiation of Debris Flow", Earth Surface Processes and Landforms, 32, 197-209, 2007.

[7] W. A. Lacerda, "Landslide initiation in saprolite and colluvium in southern Brazil: Field and laboratory observations", Geomorphology, 87 , 104-119, 2007.

[8] J. Clausen, L. Damkilde, L. Andersen, "Efficient return algorithms for associated plasticity with multiple yield planes". International Journal for Numerical Methods in Engineering, 66, 1036-1059, 2006.

[9] S.G. Bardenhagen, "Energy Conservation Error in the Material Point Method for Solid Mechanics", Journal of Computational Physics, 180, 383-403, 2002.

[10] ABAQUS—Version 6.4 2003, ABAQUS, Inc, 1080 Mainstreet Pawtucket, RI 02860-4847, 2003.